



# **OPTIMIZATION OF VARIABLE CROSS-SECTIONAL AREA THERMOELECTRIC ELEMENTS THROUGH MULTI-METHOD THERMAL-ELECTRIC COUPLED MODELING**

**Arsha K. Mamoozadeh,<sup>1</sup> Sarah E. Wielgosz,<sup>1</sup> Kevin Yu,<sup>2</sup> Fivos Drymiotis,<sup>2</sup> Matthew M. Barry<sup>1,\*</sup>**

<sup>1</sup>Department of Mechanical Engineering and Materials Science,  
University of Pittsburgh, Pittsburgh, PA 15261, USA

<sup>2</sup>Jet Propulsion Laboratory, California Institute of Technology,  
4800 Oak Grove Drive, Pasadena, CA 91109, USA

## **ABSTRACT**

A well-posed thermal-electric coupled mathematical-numerical model to optimize the cross-sectional area per length of a thermoelectric (TE) leg is introduced to maximize thermal conversion efficiency ( $\eta$ ) or power output ( $P_o$ ). To employ such optimization, the  $p$ - or  $n$ -type leg was divided into uniform length segments, wherein the product of the electrical resistance ( $R_{el}$ ) and thermal conductance ( $K$ ) was minimized as to maximize the figure of merit ( $ZT$ ) of each individual partition. The minimization of  $R_{el}K$  was dependent upon the temperature difference established across each segment, which was resolved using a one-dimensional finite difference (FD) scheme of the TE general energy equation (GEQ). The TE GEQ included all pertinent phenomena —conduction, Joule, Peltier and Thomson effects —as well as temperature dependent properties. The boundary conditions of the FD scheme were provided via a one-dimensional thermal resistance network. The current output of the uncouple was determined by the temperature bounds across the junction and the internal resistance of the TE legs, and this was explicitly coupled to the TE GEQ to create a fully-coupled model. The proposed model was validated to a fully-coupled thermal-electric finite volume method model implemented in ANSYS CFX. The proposed optimization process yielded improvements in volumetric efficiency and volumetric power output of 4.60% and 3.75%, respectively, in comparison to conventional constant-area optimization processes.

**KEY WORDS:** thermoelectric, thermal-electric coupled, multi-method modeling, optimization

## **INTRODUCTION**

Thermoelectric devices (TEDs) are a type of energy conversion apparatus that can convert a temperature difference across semiconductor materials into an electrical power output, and vice versa. When used to generate electrical power from a temperature difference across semiconductors via the Seebeck effect [1], the TED is referred to as a thermoelectric generator (TEG). TED performance is intrinsically dependent upon the  $n$ - and  $p$ -doped semiconductors that are connected electrically in series and thermally in parallel. Although the conversion efficiency is low in comparison to conventional power generation technologies such as the Rankine cycle, TEGs have several design advantages over such technologies that make them favorable for waste heat recovery and remote power generation. Namely, they are small in size with no moving parts, noiseless, emit zero-emissions, and have long operational lifetimes. Consequently, TEGs are utilized for large-scale waste heat recovery in the automotive industry, where they have been integrated into the exhaust and

\*Corresponding Matthew M. Barry: matthew.michael.barry@pitt.edu

radiator systems of automobiles to reduce fuel consumption via the conversion of heat flux into electrical power [2–5]. Other studies have used the engine as the direct heat source for a TEG system, increasing thermal conversion efficiency and power output [6, 7]. TEGs are also used to deliver power to space systems, where high-efficiency materials, lightweight design, and reliable electrical energy production are critical [8–10].

The primary reason for limited implementation of TEGs is their low thermal conversion efficiency. A thermoelectric material's maximum efficiency performance is characterized by the dimensionless figure of merit expressed as

$$Z\bar{T} = \frac{\alpha^2 \bar{T}}{\rho \lambda} \quad \text{or} \quad Z\bar{T} = \frac{\alpha^2 \bar{T}}{R_{el} K} \quad (1)$$

where  $\alpha$  is the Seebeck coefficient,  $\bar{T}$  is the average temperature across the material,  $\rho$  is the electrical resistivity,  $\lambda$  is the thermal conductivity of the material,  $R_{el}$  is electrical resistance, and  $K$  is thermal conductance [11]. The latter formulation takes into account geometric parameters. Semiconductors with increased values of  $Z\bar{T}$  are favorable because they produce more power and achieve relatively high power densities and thermal conversion efficiencies compared to other materials [12, 13]. The present work uses bismuth-telluride alloys as the material for the semiconductors [14, 15]. However, the proposed model herein is applicable to all thermoelectric (TE) materials because its objective is the optimal geometric design for the semiconductor leg regardless of TE material. In order to optimize performance, various device designs have been developed, including segmented TEGs [16–18], multi-stage TEGs [19, 20], and annular TEGs [21].

Although material properties significantly impact device performance, other factors such as device geometry and configuration are also critical. Optimization of semiconductor leg length and shape can be conducted to develop a high performing TEG. Meng et. al found that the power output of a TEG is maximized at a shorter leg length than that at which device efficiency is maximized [22]. Fabian-Mijanos and Alvarez-Quintana studied pyramidal-shaped semiconductor legs and found that maximum power output was almost two times greater than that of symmetric rectangular legs, which was accredited to the utilization of the Thomson effect [23]. While these works give insight on the effects of individual geometric parameters, the work presented herein eliminates the necessity for parametric studies by providing an algorithm that optimizes the semiconductor leg shape profile based on the realized temperature difference.

Geometric optimization of a TEG proves advantageous in several ways. Namely, it can result in a decrease in the amount of material required to construct a TEG, which will then decrease rare earth element usage. Additionally, the reduction in material results in a lighter TEG. While the difference in weight may be inconsequential upon consideration of a single uncouple, it must be considered that in practical applications, such as in the automotive or aerospace industries, hundreds of thermoelectric modules (TEMs) are required. For example, Deng et al. constructed a 115 kg TEG from 240 TEMs for application in a heavy-duty vehicle [3], and the GPHS-RTG used on the Cassini mission contained 572 SiGe junctions and weighs approximately 55.9 kg [24]. On this larger scale, reduction in weight via geometric optimization of the TEG is significant as it will improve fuel efficiency of the vehicle in automotive applications or reduce payload weight in space applications.

Previous models that have framed this work have directly analyzed the effect of thermoelectric leg geometry using cross-sectional area optimization methods to provide predictions of the leg shape profile that maximizes either thermal conversion efficiency or power output. Zare et al. optimized a segmented TEG by holding the cross section of the  $p$ -type leg constant, while optimizing the cross section of the  $n$ -type leg. In doing so, they obtained a maximum efficiency 4.98% greater than the best previously published results in a comparable temperature range [18]. Barry et al. similarly varied  $n$ -type leg geometry to optimize a single-stage TEG, though both cross-sectional area and leg length were simultaneously optimized via an analytical model. Effects of electrical and thermal contact resistances were considered in the analysis, with geometric optimization resulting in a 29% increase in volumetric power density and a 12% increase in volumetric efficiency in comparison to non-optimized geometries under comparable conditions [25]. Multi-objective and multi-parameter optimization methods have also been developed to improve TEG design. Qing et al. proposed a multi-parametric

model that optimized cross-sectional area ratio ( $A_P/L_P = A_N/L_N$ ), showing that the optimal value of ( $A_N/A_P$ ) is larger for maximum power output than it is for maximum thermal conversion efficiency [26]. He et al. produced a cross-sectional area optimization method based on the Hill-climbing algorithm that uses space trajectories throughout the optimization process to obtain maximum power output [27]. However, the Hill-climbing method is problematic in that it continuously searches for a local extrema, though it may never locate the global solution. Consequently, a genetic algorithm has been implemented for design optimization due to its application of the fundamental principles of genetics. Namely, via selection, crossover, and random mutation, the genetic algorithm searches for a better solution and surpasses the Hill-climbing method in its ability to calculate the global solution [28–30]. While the genetic algorithm is advantageous in its ability to find a global solution, it requires a large number of design evaluations, and does not provide insight into how parameters reach their optimal values. Conversely, the simplified conjugate-gradient method demonstrates how each design variable effects TEG performance through multi-objective and multi-parameter geometry optimization. Like the Hill-climbing method, it may become trapped in local minimum solutions [31, 32]. The previously mentioned optimization methods can be complicated and require significant computational time. He proposed a coupled electrical-thermal impedance matching model, in which the electrical impedance matching condition was derived for maximum power output and maximum conversion efficiency. Optimal geometry conditions are derived from the aforementioned model, which are solved in a 1D numerical model [33].

Based upon the findings of the aforementioned optimization studies, a well-posed, iterative, thermal-electric coupled analytic-numerical model is presented to conclusively determine the optimum leg shape profile that maximizes thermal conversion efficiency or power output, based upon thermal conditions and electrical load resistances. The model utilizes a one-dimensional thermal resistance network (TRN) of a thermoelectric junction, which includes thermal resistances of the interconnectors. The TRN provides the hot- and cold-side junction temperatures, which serve as the boundary conditions for a second-order central difference finite-differencing scheme of the TE general energy equation (GEQ), which governs the temperature distribution within the TE legs. The TE leg is divided into segments, where the cross-sectional area of each segment is optimized to maximize the local  $ZT$  by minimizing the  $R_{el}K$  product, which in itself is governed by the temperature gradient established across each segment as determined by the finite-differencing scheme. The electric current generated by the uncouple, based upon the realized hot- and cold-side junction temperatures and electrical resistance of the TEG legs, is coupled to the TE GEQ through the inherent source terms, which then provides updated interior boundary conditions for the TRN, thus creating a thermal-electric coupled model. By using temperature-dependent material properties for all components within the uncouple, as well as the interconnectors, an iterative solution methodology is implemented to resolve the presented system of equations. This proposed model requires one TE leg to have an invariant cross-sectional area, allowing for optimization of the cross-sectional area as a function of length of the remaining leg. Provisions for thermal and electrical contact resistances between TE materials and interconnectors can be included, but are not currently. The proposed multi-method is validated to that of a finite volume method (FVM) implemented in ANSYS CFX.

## METHODOLOGY

A schematic of a TEG uncouple is shown in Fig. 1 a). The hot-side interconnector (HSI) is exposed to a constant hot-side temperature,  $T_{\infty,h}$ , and has an associated thermal resistance  $R_{th,int,h}$ , as shown in Fig. 1 b). The hot-sides of the  $p$ - and  $n$ -type materials are in contact with the bottom of the HSI and the temperatures at the interface of these materials is assumed equal, and is denoted as one variable  $T_{N,h} = T_{P,h} = T_h$ . The heat entering the HSI is denoted as  $Q_h$ , and is solved for via the application of a TRN to the hot-side interconnector such that:

$$Q_h = \frac{T_{\infty,h} - T_h}{\tilde{R}_{th,int,h}}. \quad (2)$$

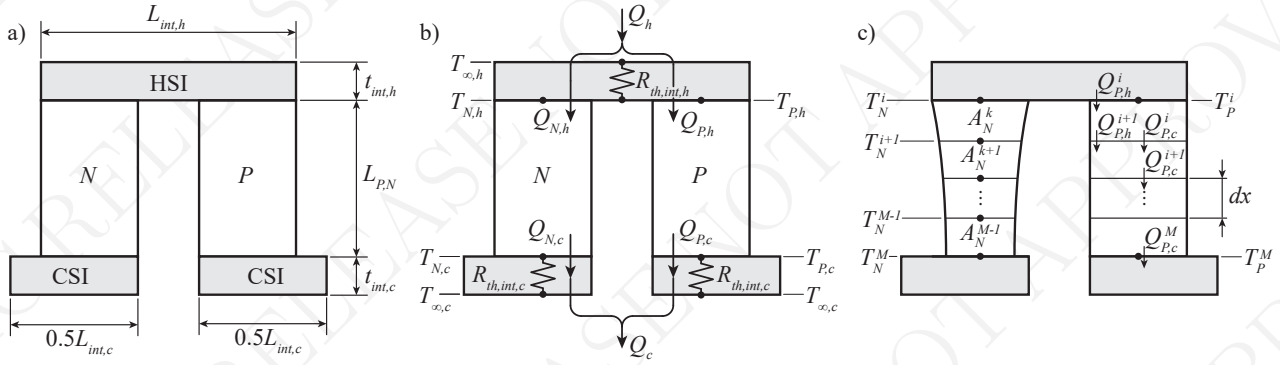


**Fig. 1** Schematic of TEG uncouple with a) prescribed geometry, b) nodal temperature values and bounds, thermal resistances of HSI and CSI, and heats for TRN, and c) discretized  $n$ - and  $p$ -type legs with slice temperatures and heat flows.

The thermal resistance of the HSI is expressed in terms of the length of the interconnector,  $L_{int}$  taken in the vertical direction, per the product of integral average of the thermal conductivity, denoted  $\tilde{\lambda}_{int,h}$ , and the cross-sectional area, denoted  $A_{int,h}$ , such that

$$\tilde{R}_{th,int,h} = \frac{L_{int,h}}{\tilde{\lambda}_{int,h} A_{int,h}}. \quad (3)$$

The heat entering the hot-side interconnector must also be the sum of the heat entering the hot-side of the  $p$ - and  $n$ -type legs, which is given by [34] as:

$$Q_{N,h} = \alpha_N(T_{N,h})IT_{N,h} + \tilde{K}_N(T_{N,h} - T_{N,c}) - \frac{I}{2} \left( I\tilde{R}_{el,N} + \tilde{\tau}_N(T_{N,h} - T_{N,c}) \right) \quad (4)$$

$$Q_{P,h} = \alpha_P(T_{P,h})IT_{P,h} + \tilde{K}_P(T_{P,h} - T_{P,c}) - \frac{I}{2} \left( I\tilde{R}_{el,P} + \tilde{\tau}_P(T_{P,h} - T_{P,c}) \right). \quad (5)$$

Within Eqns. 4 and 5,  $\alpha_{N,P}$  is the Seebeck coefficient evaluated at the hot-side temperature.  $I$  is the magnitude of the current density vector, which is defined after the remaining terms.  $\tilde{K}$  is the integral-averaged thermal conductance evaluated between the hot- and cold-side material temperatures,  $T_h$  and  $T_c$ , and is expressed as

$$\tilde{K}_{N,P} = \sum_{i=1}^{M-1} \frac{\tilde{\lambda}_{N,P}^k A_{N,P}^k}{L_{N,P}^k} \quad (6)$$

where  $\tilde{\lambda}_{N,P}^k$  is the integral-averaged thermal conductivity of each slice evaluated between the temperatures of  $T_i$  and  $T_{i+1}$ ,  $A_{N,P}^k$  is the cross-sectional area of each slice and  $L_{N,P}^k$  is the length of the  $n$ - and  $p$ -type materials of each slice. Similarly,  $\tilde{R}_{el,N,P}$  is the electrical resistance of the  $n$ - and  $p$ -materials expressed as

$$\tilde{R}_{el,N,P} = \sum_{i=1}^M \frac{\tilde{\rho}_{N,P}^k L_{N,P}^k}{A_{N,P}^k} \quad (7)$$

where  $\tilde{\rho}_{N,P}^k$  is the integral-averaged electrical resistivity of each slice. Lastly,  $\tilde{\tau}_{N,P}$  is the integral-averaged

Thomson coefficient, which is expressed as

$$\tau_{N,P} = \left( \frac{\partial \alpha_{N,P}}{\partial T} \right) T. \quad (8)$$

The temperature at the cold-side of the  $n$ - and  $p$ -type materials is assumed to be the same, and thus  $T_{N,c} = T_{P,c} = T_c$ . The heat exiting the legs must sum to the heat exiting both of the cold-side interconnectors (CSI), and the heat exiting  $n$ - and  $p$ -type materials is provided by [34], which is expressed as

$$Q_{N,c} = \alpha_N(T_{N,c})IT_{N,c} + \tilde{K}_N(T_{N,h} - T_{N,c}) + \frac{I}{2} \left( I\tilde{R}_{el,N} + \tilde{\tau}_N(T_{N,h} - T_{N,c}) \right) \quad (9)$$

$$Q_{P,c} = \alpha_P(T_{P,c})IT_{P,c} + \tilde{K}_P(T_{P,h} - T_{P,c}) + \frac{I}{2} \left( I\tilde{R}_{el,P} + \tilde{\tau}_P(T_{P,h} - T_{P,c}) \right). \quad (10)$$

Within Eqns. 9 and 10,  $\alpha_{N,P}$  is the Seebeck coefficient evaluated at the cold-side temperature. Finally, the heat exiting the CSI is expressed as

$$Q_c = \frac{T_c - T_{\infty,c}}{\tilde{R}_{th,int,c}}. \quad (11)$$

The thermal resistance of the CSI is defined as

$$\tilde{R}_{th,int,c} = \frac{L_{int,c}}{\tilde{\lambda}_{int,c}A_{int,c}}. \quad (12)$$

All temperature-dependent thermophysical properties listed in Eqns. 2 through 12 are represented as polynomial functions in Tab. 1. When the  $n$ - and  $p$ -type legs are discretized into equal length slices as show in Fig. 1 c), the value of  $M - 1$  in Eqns. 6 and 7 is the number of slices in the thermoelectric element leg. In order to calculate the integral average of the material properties of these slices, the intermediate temperatures between the slices must be resolved. Additionally, Eqns. 4, 5, 9 and 10 are still applicable as to determine the heat entering and exiting each slice, and the temperatures and temperature bounds within said equations are modified to reflect those across the slice. To accomplish the resolution of the temperatures at the interface of each slice, the steady-state GEQ taking into account conduction, Joule and Thomson heating, and the Peltier effect for the semiconductors is employed. The GEQ [35] is expressed as

$$\nabla \cdot (\lambda A \nabla T) + \rho A \mathbf{J}^2 - T A \mathbf{J} \left[ (\nabla \alpha)_T + \left( \frac{\partial \alpha}{\partial T} \right) \nabla T \right] - \alpha T \nabla \mathbf{J} = 0 \quad (13)$$

where the first term represents conduction through a non-uniform member, the second term is the Joule heat, the third term is the Peltier heat, the fourth term is the Thomson heat, and the fifth term is the Bridgman heat. The GEQ is considered in one-dimension—the axial direction. The Bridgman heat is neglected, for the current density vector  $\mathbf{J}$  in one dimension is represented as a scalar value. The magnitude of  $\mathbf{J}$  is expressed as the scalar value of current,  $I$ , per the cross-sectional area of the slice,  $A$ . The Peltier effect is not included in the one-dimensional representation of the GEQ, for it occurs only at the interface of the thermoelectric material and interconnectors. Thus, Eqn. 13 is represented in the axial direction as

$$\frac{\partial}{\partial x} \left( \lambda A \left( \frac{\partial T}{\partial x} \right) \right) + \frac{\rho I^2}{A} - T I \left( \frac{\partial \alpha}{\partial T} \right) \frac{\partial T}{\partial x} = 0. \quad (14)$$

Thus, after applying the product rule within the conduction term, and using Eqn. 8 within the third term of Eqn.14, the following is obtained

$$\frac{d\lambda}{dx} A \frac{dT}{dx} + \lambda A \frac{d^2T}{dx^2} + \lambda \frac{dA}{dx} \frac{dT}{dx} + \frac{\rho I^2}{A} - \tau I \frac{dT}{dx} = 0. \quad (15)$$

The cross-sectional area of the  $n$ - or  $p$ -type leg slice was averaged based upon the cross-sectional area of point  $i$  and  $i + 1$  during the differencing scheme such that

$$A_i = \frac{A_i + A_{i+1}}{2}. \quad (16)$$

With Eqn. 16 defined, a second-order accurate central differencing finite differencing scheme is applied to Eqn. 15. In doing such, Eqn. 15 is expressed as

$$\begin{aligned} & \left( \frac{\lambda_{i+1} - \lambda_{i-1}}{2\Delta x} \right) A_i \left( \frac{T_{i+1} - T_{i-1}}{2\Delta x} \right) + \lambda_i A_i \left( \frac{T_{i+1} - 2T_i + T_{i-1}}{\Delta x^2} \right) + \dots \\ & \dots \lambda_i \left( \frac{A_{i+1} - A_{i-1}}{2\Delta x} \right) \left( \frac{T_{i+1} - T_{i-1}}{2\Delta x} \right) + \frac{\rho_i I^2}{A_i} - \tau I \left( \frac{T_{i+1} - T_{i-1}}{2\Delta x} \right) = 0. \end{aligned} \quad (17)$$

The temperature at the intermediate interfaces of each leg,  $T_i$ , is solved as

$$\begin{aligned} T_i = & \left( \frac{\Delta x^2}{2\lambda_i A_i} \right) \left( \left( \frac{\lambda_{i+1} - \lambda_{i-1}}{4\Delta x^2} A_i + \frac{\lambda A_i}{\Delta x^2} + \lambda_i \frac{A_{i+1} - A_{i-1}}{4\Delta x^2} + \frac{\tau I}{2\Delta x} \right) T_{i+1} + \dots \right. \\ & \left. \dots \left( - \left( \frac{\lambda_{i+1} - \lambda_{i-1}}{4\Delta x^2} \right) A_i + \frac{\lambda A_i}{\Delta x^2} - \lambda_i \left( \frac{A_{i+1} - A_{i-1}}{4\Delta x^2} \right) - \frac{\tau I}{2\Delta x} \right) T_{i-1} + \frac{\rho I^2}{A_i} \right) \end{aligned} \quad (18)$$

The variable  $I$  is calculated from the open-circuit voltage,  $V_{oc}$ , and the internal and load resistance,  $R_{in}$  and  $R_{load}$ , respectively. Thus,  $I$  is expressed as

$$I = \frac{V_{oc}}{R_{in} + R_{load}} = \frac{(|\tilde{\alpha}_N| + \tilde{\alpha}_P)(T_h - T_c)}{\tilde{R}_{el,N} + \tilde{R}_{el,P} + R_{load}} \quad (19)$$

where both the integral-average Seebeck coefficient is evaluated and the electrical resistance is calculated on a per-slice basis. The load resistance was set to either of two values, as to either maximize power output or to maximize efficiency:

$$R_{load} = \begin{cases} R_{in} & \text{maximize power output} \\ R_{in} \left( 1 + \left( \frac{(|\tilde{\alpha}_N| + \tilde{\alpha}_P)^2}{[(\tilde{\rho}_N \tilde{\lambda}_N)^{\frac{1}{2}} + (\tilde{\rho}_P \tilde{\lambda}_P)^{\frac{1}{2}}]^2} \right) \left( \frac{T_c + T_h}{2} \right) \right)^{\frac{1}{2}} & \text{maximize efficiency} \end{cases} \quad (20)$$

Once the temperatures at each slice interface are determined, the ratio of cross-sectional areas of the  $n$ - and

$p$ -type materials can be optimized based upon the formulation provided by Angrist [11] such that

$$\frac{A_N}{A_P} = \begin{cases} \left( \frac{\tilde{\rho}_N}{\tilde{\rho}_P} \right)^{\frac{1}{2}} & \text{maximize power output} \\ \left( \frac{\tilde{\rho}_N \tilde{\lambda}_N}{\tilde{\rho}_P \tilde{\lambda}_P} \right)^{\frac{1}{2}} & \text{maximize efficiency} \end{cases} \quad (21)$$

The system response quantities (SRQs), namely power output, denoted as  $P_o$ , and efficiency, denoted as  $\eta$ , are calculated as follows. The power output is expressed as

$$P_o = I^2 R_{load}. \quad (22)$$

The efficiency is expressed as

$$\eta = \frac{P_o}{Q_h} \quad (23)$$

To optimize the cross-sectional area, the following solution algorithm is implemented. This methodology is illustrated in Fig. 2.

1. The cross-sectional areas of both the  $n$  and  $p$ -type materials are initialized with a reasonable value (e.g. 25 mm<sup>2</sup>), and the bounding and interfacial temperatures of the thermoelectric materials are prescribed as to populate Eqns. 2 and 11. The value for current is initialized as zero.
2. Using the prescribed temperature values, as well as the free-stream temperatures across the TEG, material properties of the interconnector and thermoelectric materials are defined on a per-slice basis, namely  $\tilde{\lambda}_{int,h}$  in Eqn. 3,  $\tilde{\lambda}_{N,P}$  in Eqn. 6,  $\tilde{\rho}_{N,P}$  in Eqn. 7,  $\tilde{\tau}_{N,P}$  as defined by Eqn. 8, and  $\tilde{\lambda}_{int,c}$  in Eqn.12.
3. The temperatures at the interfaces of the slices are then calculated via Eqn. 18 considering Eqn. 16.
4. Next,  $T_h$  is solved for using the continuity of heat via Eqns. 2, 4 and 5, and  $T_c$  is solved for using the continuity of heat via Eqns. 9, 10 and 11.
5. The cross-sectional area of one of the legs is then optimized on a per-slice basis using Eqn. 21.
6. Then the current is calculated via Eqn. 19, and is used to re-initialize the aforementioned system of equations. This process is repeated until there is convergence of temperatures, heat, and current to a residual criteria of a maximum of 1e-10.
7. Once all SRQs reach the specified convergence criteria,  $R_{load}$  as defined by Eqn. 20 is calculated and used to determine  $P_o$  as defined by Eqn. 22 and  $\eta$  as defined by Eqn. 23.

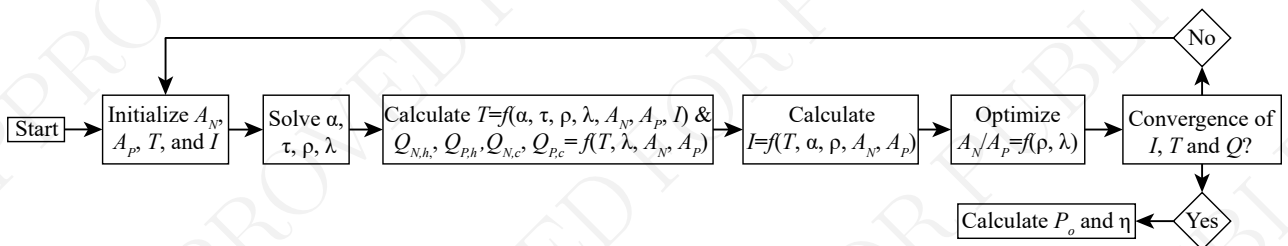


**Fig. 2** Iterative solution algorithm.

**Table 1** Polynomial expressions for temperature dependent thermoelectric and interconnector properties.

<i>n</i> -type Bi <sub>2</sub> Te <sub>1.9</sub> Se <sub>1.1</sub> [15]		<i>p</i> -type Ge <sub>0.7</sub> Pb <sub>0.13</sub> Te+3% Bi <sub>2</sub> Te <sub>3</sub> [14]	
$\alpha_N$	$= (-3.202118465009907e-19)T^6 + (9.203585371307136e-16)T^5 + (-1.073152310161369e-12)T^4 + (6.493910899794523e-10)T^3 + (-2.15109875689092e-7)T^2 + (3.646981516744837e-5)T + (-0.002561458547361978)$	$\alpha_P$	$= (-1.500813826446285e-19)T^6 + (4.293338680148655e-16)T^5 + (-5.014714714245148e-13)T^4 + (3.042590912073281e-10)T^3 + (-1.010501330398025e-7)T^2 + (1.822883155906853e-5)T + (-0.001365897370156843)$
$\lambda_N$	$= (3.634218867237926e-15)T^6 + (-1.119227631273517e-11)T^5 + (1.410461035072385e-8)T^4 + (-9.307231318913803e-6)T^3 + (0.003396895991439032)T^2 + (-0.6552982139209359)T + (54.70633936832369)$	$\lambda_P$	$= (5.238086549608868e-17)T^6 + (-2.927636770231909e-13)T^5 + (5.844390241944433e-10)T^4 + (-5.642804450717544e-7)T^3 + (0.0002909446395983974)T^2 + (-0.08063418038142083)T + (11.00293123390308)$
$\sigma_N$	$= (-3.253703447464733e-8)T^5 + (8.721294302777075e-5)T^4 + (-0.09344706416614766)T^3 + (50.97626108178136)T^2 + (-14667.25239632805)T + (1892814.656277739)$	$\sigma_P$	$= (1.319288092705862e-10)T^6 + (-3.85669843140294e-7)T^5 + (0.0004638862454473422)T^4 + (-0.297110247163325)T^3 + (109.4552349385509)T^2 + (-22997.10238999909)T + (2309068.907784006)$
Interconnectors - Copper			
$\lambda_{int}$	$= (1.5625e-5)T^2 - (8.5625e-2)T + 4.0555e+2$		
$\rho_{int}$	$= (6.7872e-11)T - 3.0865e-9$		

## RESULTS AND DISCUSSION

For the optimization of the leg shape profile when solving for either maximum  $\eta$  or  $P_o$ , the *p*-type material cross-sectional area was varied, while the length for both *n*- and *p*-type materials, as well as the cross-sectional area for the *n*-type material, were held constant. The cold- and hot-side interconnectors had a length of 1 mm, and the area was taken as 2.5 times the maximum of the *p*- and *n*-type materials cross-sectional areas. The cold-side temperature  $T_{\infty,c}$  was fixed at 300 K and the hot-side temperature  $T_{\infty,h}$  was fixed at 700 K.

### 3.1 Validation

The proposed analytic model was validated to a fully-coupled three-dimensional FVM model implemented in ANSYS CFX [36]. A non-optimized (constant cross-section) and optimized case were individually compared to the numeric models, and the percent differences of SRQs are presented in Tab. 2. The geometrical inputs for the analytic and numeric models are as follows - the *p* and *n*-type materials had a leg length of 10 mm and the *p* and *n*-type material had cross-sectional areas of 25 mm<sup>2</sup>.

The optimized model used in the validation study was studied to determine the requisite number of slices needed to achieve a grid independent solution, as shown in Tab. 3. Once again, the leg lengths of the *p* and *n*-type materials were held invariant at 10 mm, and the cross-sectional area of the *n*-type was fixed at 25 mm<sup>2</sup>. The cross-sectional area of the *p*-type material was then optimized. Once the number of slices equals or exceeds 256, the percent difference between successive refinements remains below 1e-3 for all variables of interest, and said value is used for all remaining analyses. It is noted in Tab. 3 that the scenario of the



**Table 2** Validation of analytic model to fully-coupled FVM model with  $T_{\infty,c}=300$  K,  $T_{\infty,h}=700$  K, and solving for maximum power.

SRQ	Non-optimized			Optimized		
	Numeric	Analytic	% Diff.	Numeric	Analytic	% Diff.
$Q_h$	4.160 090	4.169 074	0.22	4.506 100	4.528 489	0.50
$V_{oc}$	0.192 091	0.192 941	0.44	0.192 226	0.192 954	0.38
$I$	4.914 890	4.920 140	0.11	5.372 490	5.415 763	0.80
$R_{in}$	0.019 542	0.019 607	0.33	0.017 890	0.017 814	0.42
$P_o$	0.472 052	0.474 648	0.55	0.516 367	0.522 497	1.18
$\eta$	11.347 200	11.384 972	0.33	11.459 300	11.537 998	0.68

legs being represented by a singular slice is reflective of the conventional cross-sectional area optimization proposed by [11]. Even for the validation case, when optimizing the cross-sectional area as a function of length, the power output increases 1.65% in comparison to the conventionally optimized scenario ( $M=1$ ), and 11.43% in comparison to the non-optimized case. The cross-sectional area as a function of number of slices is portrayed in Fig. 3 a), where  $A_P$  is plotted against the leg length. Figure 3 b) provides a depiction of the medium mesh used within the numerical validation, as well as the shape profile of the  $p$ -type leg in comparison to the  $n$ -type leg.

**Table 3** Grid independence study of optimized geometry model with  $T_{\infty,c}=300$  K,  $T_{\infty,h}=700$  K for all SRQ with reported percent difference, solving for maximum power.

No. Slices	$Q_h$	% Diff.	$R_{in}$	% Diff.	$V_{oc}$	% Diff.	$I$	% Diff.
1	4.608 755		0.018105		0.192951		5.328661	
2	4.575 990	7.13E-1	0.017 680	2.37E+0	0.192 952	7.42E-4	5.456 645	2.37E+0
4	4.543 042	7.23E-1	0.017 767	4.89E-1	0.192 954	6.56E-4	5.430 089	4.88E-1
8	4.533 104	2.19E-1	0.017 797	1.70E-1	0.192 954	1.97E-4	5.420 893	1.70E-1
16	4.530 376	6.02E-2	0.017 806	4.76E-2	0.192 954	5.41E-5	5.418 317	4.75E-2
32	4.529 671	1.56E-2	0.017 808	1.24E-2	0.192 954	1.40E-5	5.417 645	1.24E-2
64	4.529 482	4.16E-3	0.017 809	3.48E-3	0.192 954	3.73E-6	5.417 457	3.48E-3
128	4.529 391	2.01E-3	0.017 809	2.27E-3	0.192 954	1.78E-6	5.417 334	2.27E-3
256	4.529 193	4.37E-3	0.017 810	6.20E-3	0.192 954	3.83E-6	5.416 998	6.20E-3
512	4.528 443	1.66E-2	0.017 814	2.43E-2	0.192 954	1.45E-5	5.415 681	2.43E-2

The uncertainty associated with casting the set of partial differential equations into a finite volume formulation via the process of discretization was quantified through the use of a grid convergence index (GCI) as defined by [37] and modified by Oberkampf and Roy [38]. This GCI value represents the numeric uncertainty,  $U_{num}$ , associated with each SRQ, and is the gold standard of the American Society of Mechanical Engineers. Three successively refined meshes were used in the determination of the GCI and subsequent numeric uncertainty, which represent a 95% confidence interval, with the details provided by Celik [39]. The coarse mesh consisted of 117,404 cells, the medium 1,102,500 cells, and the fine 9,366,836 cells. Furthermore, the values in Tab. 4 indicate a grid independent solution was obtained.

To ascertain the device efficiency and power output improvement, the results for optimizing the cross-sectional area as a function of length were compared to the standard constant cross-sectional area optimization procedure (i.e. when  $M=1$ ). These results are shown in Fig. 4 below.

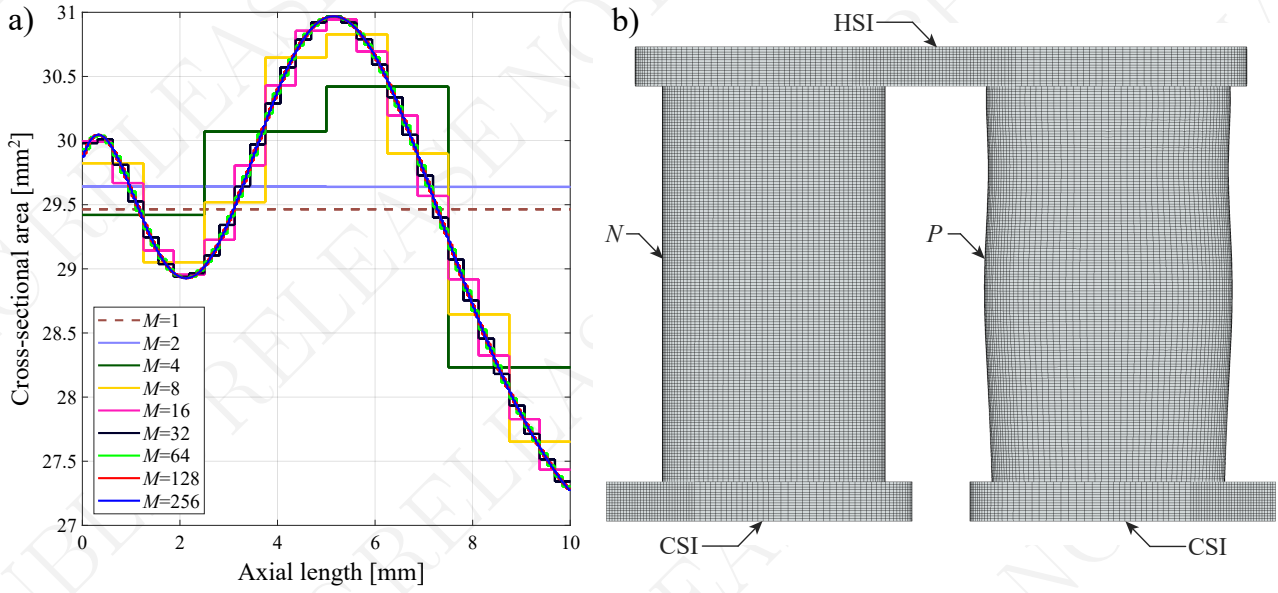


**Fig. 3** Representation of a) cross-sectional area shape profile of the *p*-type material as a function of number of slices, and b) the medium mesh of the optimized *p*-type leg used within the validating numerical model.

**Table 4** Grid independence and discretization uncertainty study of optimized geometry model with  $T_{\infty,c}=300$  K,  $T_{\infty,h}=700$  K for all SRQ, solving for maximum power.

SRQ	Coarse	Medium	Fine	GCI	$U_{num}$
$Q_h$	4.488 260	4.494 320	4.506 100	0.033	0.73
$V_{oc}$	0.196 126	0.191 019	0.192 226	4.77e-4	0.25
$I$	5.421 820	5.361 940	5.372 490	0.010	0.19
$R_{in}$	0.017 713	0.017 813	0.017 890	5.39e-4	3.01
$P_o$	0.520 695	0.512 116	0.516 367	0.013	2.53
$\eta$	11.601 300	11.394 700	11.459 300	0.094	0.82

In Fig. 4 a), the height of the TEM is varied between 1 and 10 mm in 1 mm increments, while the cross-sectional area of the *n*-type is held invariant at 25 mm<sup>2</sup>. While varying the height of the TEM, maximum power output is obtained via the aforementioned optimization processes. Fig. 4 b) varies the cross-sectional area of the *n*-type material from 1 to 25 mm<sup>2</sup>, while the height of the TEM is held invariant at 10 mm. At discrete points in this range, the cross-sectional area of the *p*-type leg is optimized along the length of the leg to yield maximum power output. Figures 4 c) and d) depict the results of the optimization process for achieving maximum efficiency using the same geometric ranges of Figs. 4 a) and b), respectively.

It is seen throughout the optimization process to maximize power output that there are minimal gains. For instance, when the height of the TEM is 1 mm, the variable cross-sectional area optimization increases the power output by 2.26% in comparison to the conventionally optimized geometry. This increase in power output decreases with increase in leg height, as seen in Fig. 4 a), decreasing to a value of 1.66%. Changing the seed area of the *n*-type leg had the opposite effect of increasing TEM height; there was an increase in power output as the seed area increased, as seen in Fig. 4 b). The improvement in power output increases from 1.58% to 1.66% - an insignificant amount. Although the system performance shown in Figs. 4 a) and b) was generated by optimizing the power output, the thermal conversion efficiency of the cross-sectional area optimized devices are consistently better than conventionally optimized devices by an average of 3.50%.

When maximizing thermal conversion efficiency, the variable cross-sectional area optimization near uniformly

increases said SRQ across the entire range of TEM heights, as seen in Fig. 4 c). The thermal conversion efficiency increases by 4.48% when the TEM height is taken as 1 mm, and this increase diminishes to a value of 4.33% when the TEM height is taken as 10 mm. Additionally, changing the seed area of the  $n$ -type leg has minimal effect on thermal conversion efficiency, but the efficiency improvement diminished as the seed area decreased, as seen in Fig. 4 d). The average improvement in thermal conversion efficiency was found to be 4.32%. It is noted that the power output increased on average 3.37% over the range of TEM heights and 3.26% over the range of  $n$ -type areas when optimizing thermal conversion efficiency.

Lastly, there are appreciable improvements in volumetric efficiency and volumetric power output, i.e. the thermal conversion efficiency and power output normalized to the volume of thermoelectric material. In the situation of maximizing thermal conversion efficiency while varying TEM height, there is a maximum increase in volumetric thermal conversion efficiency of 4.60%, in comparison to the 4.48% increase in thermal conversion efficiency, and a 3.75% in volumetric power output, in comparison to the 3.63% increase in power output. Similarly, in the situation of maximizing thermal conversion efficiency but varying the seed area of the  $n$ -type material, the maximum volumetric thermal conversion efficiency and power output improvements are found to be 4.42% and 3.37%, respectively, in comparison to thermal conversion efficiency and power output value improvements of 4.33% and 3.29%, respectively.

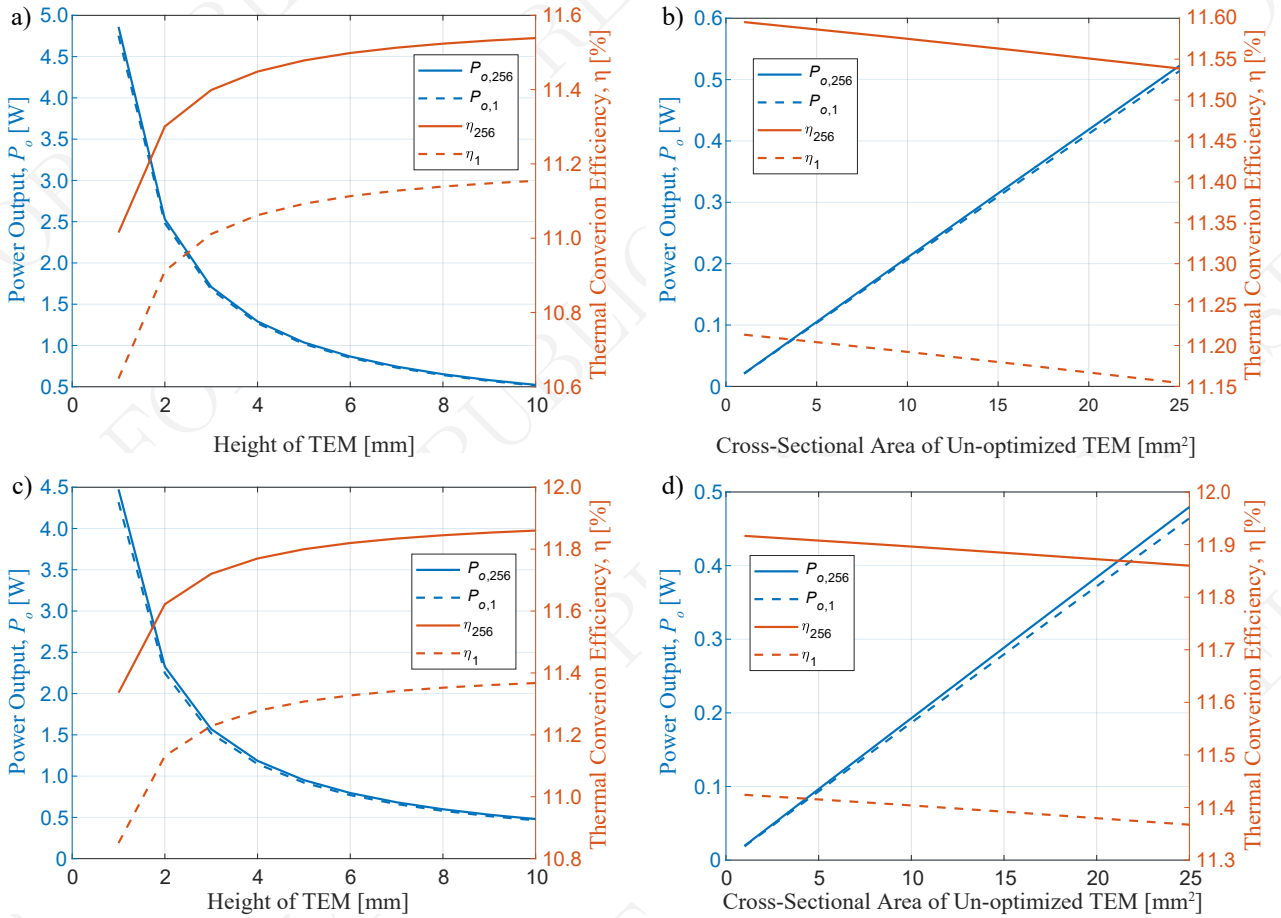


**Fig. 4** Maximization of power out,  $P_o$ , for varying a) TEM height and b)  $n$ -type area, and thermal conversion efficiency,  $\eta$ , for varying c) TEM height and d)  $n$ -type area. Conventionally optimized geometry denoted by dashed lines and a subscript of unity, and cross-sectional area optimization along leg length values denoted by subscript 256.

## CONCLUSIONS

A thermal-electric coupled mixed-method algorithm that predicts TEG performance and optimizes the cross-sectional area along the leg length in order to optimize power output or thermal conversion efficiency was introduced, validated and demonstrated over a range of TEM geometries. The primary result from the presented variable cross-sectional area optimization algorithm is that the proposed method always improved the power output and the thermal conversion efficiency compared to a conventionally optimized device. Through the implementation of the aforementioned algorithm in a limited design space, the maximum power output and thermal conversion efficiency improvements of a cross-sectional area optimized TEG, in comparison to a conventionally optimized TEG, were 2.26% and 4.48%, respectively, when said quantities were the objective of the optimization method. The maximum attainable increases power output and thermal conversion efficiency were 3.75% and 4.60%, respectively, in comparison to a conventionally optimized TEG, when said quantities were normalized to the volume of thermoelectric material.

## NOMENCLATURE

### Variables

$A$	area	(m <sup>2</sup> )	$P_o$	power output	(W)
$I$	current	(A)	$Q$	heat	(W)
$\mathbf{J}$	current density vector	(Am <sup>-2</sup> )	$R$	resistance, electrical or thermal	( $\Omega$ or KW <sup>-1</sup> )
$K$	thermal conductance	(WK <sup>-1</sup> )	$T$	temperature	(K)
$L$	Length	(m)	$U_{\text{num}}$	numeric uncertainty	(%)
$M$	number	(-)	$\forall$	volume	(m <sup>3</sup> )
$N$	$n$ -type		$V_{oc}$	open-circuit voltage	(V)
$P$	$p$ -type		$ZT$	dimensionless figure of merit	(-)

### Subscripts and Superscripts

$c$	cold-side	$int$	interconnector
$el$	electrical	$k$	indices
$h$	hot-side	$load$	load
$i$	indices	$N$	$n$ -type
$in$	internal	$P$	$p$ -type
$\infty$	free-stream	$th$	thermal

### Greek Letters

$\alpha$	Seebeck coefficient	(VK <sup>-1</sup> )	$\rho$	electrical resistivity	( $\Omega\text{m}$ )
$\eta$	thermal conversion efficiency	(-)	$\sigma$	electrical conductivity	(Sm <sup>-1</sup> )
$\lambda$	thermal conductivity	(Wm <sup>-1</sup> K <sup>-1</sup> )	$\tau$	Thomson coefficient	(VK <sup>-1</sup> )

### Acronyms

CSI	cold-side interconnector	SRQ	system response quantity
FD	finite difference	TE	thermoelectric
FVM	finite volume method	TED	thermoelectric device
GCI	grid convergence index	TEG	thermoelectric generator
GEQ	general energy equation	TEM	thermoelectric module
HSI	hot-side interconnector	TRN	thermal resistance network

## REFERENCES

- [1] T. J. Seebeck, "Ueber die magnetische polarisation der metalle und erze durch temperaturdifferenz," *Annalen der Physik*, vol. 82, no. 3, pp. 253–286, 1826.
- [2] R. Rodriguez, M. Preindl, J. S. Cotton, and A. Emadi, "Review and trends of thermoelectric generator heat recovery in automotive applications," *IEEE Transactions on Vehicular Technology*, 2019.
- [3] Y. Deng, T. Hu, C. Su, and X. Yuan, "Fuel economy improvement by utilizing thermoelectric generator in heavy-duty vehicle," *Journal of Electronic Materials*, vol. 46, no. 5, pp. 3227–3234, 2017.
- [4] S. Kumar, S. D. Heister, X. Xu, J. R. Salvador, and G. P. Meisner, "Thermoelectric generators for automotive waste heat recovery systems part i: Numerical modeling and baseline model analysis," *Journal of electronic materials*, vol. 42, no. 4, pp. 665–674, 2013.
- [5] S. Kumar, S. D. Heister, X. Xu, J. R. Salvador, and G. P. Meisner, "Thermoelectric generators for automotive waste heat recovery systems part ii: Parametric evaluation and topological studies," *Journal of electronic materials*, vol. 42, no. 6, pp. 944–955, 2013.
- [6] Y. Zhang, M. Cleary, X. Wang, N. Kempf, L. Schoensee, J. Yang, G. Joshi, and L. Meda, "High-temperature and high-power-density nanostructured thermoelectric generator for automotive waste heat recovery," *Energy Conversion and Management*, vol. 105, pp. 946–950, 2015.
- [7] T. Y. Kim, A. A. Negash, and G. Cho, "Waste heat recovery of a diesel engine using a thermoelectric generator equipped with customized thermoelectric modules," *Energy Conversion and Management*, vol. 124, pp. 280–286, 2016.
- [8] M. S. El-Genk, H. H. Saber, and T. Caillat, "Efficient segmented thermoelectric uncouples for space power applications," *Energy Conversion and Management*, vol. 44, pp. 1755–1772, 2003.
- [9] R. O'Brien, R. Ambrosi, N. Bannister, S. Howe, and H. V. Atkinson, "Safe radioisotope thermoelectric generators and heat sources for space applications," *Journal of Nuclear Materials*, vol. 377, no. 3, pp. 506–521, 2008.
- [10] C. S. Matthes, D. F. Woerner, T. J. Hendricks, J.-P. Fleurial, K. I. Oxnevad, C. D. Barklay, and J. F. Zakrajsek, "Next-generation radioisotope thermoelectric generator study," in *2018 IEEE Aerospace Conference*, pp. 1–9, IEEE, 2018.
- [11] S. W. Angrist, *Direct Energy Conversion*. Allyn and Bacon Inc. (Boston), 4 ed., 1982.
- [12] E. Altenkirch, "Über den nutzeffekt der thermosäule," *Physikalische Zeitschrift*, vol. 10, pp. 560–580, 1909.
- [13] E. Altenkirch, "Elektrothermische kälteerzeugung und reversible elektrische heizung," *Physikalische Zeitschrift*, vol. 12, pp. 920–924, 1911.
- [14] D. Wu, L.-D. Zhao, S. Hao, Q. Jiang, F. Zheng, J. W. Doak, H. Wu, H. Chi, Y. Gelbstein, C. Uher, *et al.*, "Origin of the high performance in gete-based thermoelectric materials upon bi2te3 doping," *Journal of the American Chemical Society*, vol. 136, no. 32, pp. 11412–11419, 2014.
- [15] Z. Tang, L. Hu, T. Zhu, X. Liu, and X. Zhao, "High performance n-type bismuth telluride based alloys for mid-temperature power generation," *Journal of Materials Chemistry C*, vol. 3, no. 40, pp. 10597–10603, 2015.
- [16] H. Tian, X. Sun, Q. Jia, X. Liang, G. Shu, and X. Wang, "Comparison and parameter optimization of a segmented thermoelectric generator by using the high temperature exhaust of a diesel engine," *Energy*, vol. 84, pp. 121–130, 2015.
- [17] H. Ali and B. S. Yilbas, "Configuration of segmented leg for the enhanced performance of segmented thermoelectric generator," *International Journal of Energy Research*, vol. 41, no. 2, pp. 274–288, 2017.
- [18] M. Zare, H. Ramin, S. Naemi, and R. Hosseini, "Exact optimum design of segmented thermoelectric generators," *International Journal of Chemical Engineering*, vol. 2016, 2016.
- [19] R. Arora and R. Arora, "Multicriteria optimization based comprehensive comparative analyses of single-and two-stage (series/parallel) thermoelectric generators including the influence of thomson effect," *Journal of Renewable and Sustainable Energy*, vol. 10, no. 4, p. 044701, 2018.
- [20] M. Zhou, Y. He, and Y. Chen, "Three-dimensional numerical modeling and characterization of two-stage and multilayer thermoelectric couples," *International Journal of Green Energy*, vol. 13, no. 7, pp. 736–746, 2016.
- [21] A. Zhang, B. Wang, D. Pang, J. Chen, J. Wang, and J. Du, "Influence of leg geometry configuration and contact resistance on the performance of annular thermoelectric generators," *Energy Conversion and Management*, vol. 166, pp. 337–342, 2018.
- [22] J.-H. Meng, X.-X. Zhang, and X.-D. Wang, "Characteristics analysis and parametric study of a thermoelectric generator by considering variable material properties and heat losses," *International Journal of Heat and Mass Transfer*, vol. 80, pp. 227–235, 2014.
- [23] A. Fabian-Mijangos and J. Alvarez-Quintana, "Thermoelectric devices: Influence of the legs geometry and parasitic contact resistances on  $z_t$ ," in *Bringing Thermoelectricity into Reality*, IntechOpen, 2018.
- [24] G. Bennett, J. Lombardo, R. Hemler, G. Silverman, C. Whitmore, W. Amos, E. Johnson, A. Schock, R. Zocher, T. Keenan, *et al.*, "Mission of daring: the general-purpose heat source radioisotope thermoelectric generator," in *4th International Energy Conversion Engineering Conference and Exhibit (IECEC)*, p. 4096, 2006.
- [25] M. M. Barry, K. A. Agbim, P. Rao, C. E. Clifford, B. Reddy, and M. K. Chyu, "Geometric optimization of thermoelectric

- elements for maximum efficiency and power output,” *Energy*, vol. 112, pp. 388–407, 2016.
- [26] S. Qing, A. Rezaia, L. A. Rosendahl, and X. Gou, “An analytical model for performance optimization of thermoelectric generator with temperature dependent materials,” *Ieee Access*, vol. 6, pp. 60852–60861, 2018.
  - [27] H. He, Y. Wu, W. Liu, M. Rong, Z. Fang, and X. Tang, “Comprehensive modeling for geometric optimization of a thermoelectric generator module,” *Energy Conversion and Management*, vol. 183, pp. 645–659, 2019.
  - [28] L. Zhu, H. Li, S. Chen, X. Tian, X. Kang, X. Jiang, and S. Qiu, “Optimization analysis of a segmented thermoelectric generator based on genetic algorithm,” *Renewable Energy*, 2020.
  - [29] W.-H. Chen, P.-H. Wu, and Y.-L. Lin, “Performance optimization of thermoelectric generators designed by multi-objective genetic algorithm,” *Applied Energy*, vol. 209, pp. 211–223, 2018.
  - [30] H. Sun, Y. Ge, W. Liu, and Z. Liu, “Geometric optimization of two-stage thermoelectric generator using genetic algorithms and thermodynamic analysis,” *Energy*, vol. 171, pp. 37–48, 2019.
  - [31] J.-H. Meng, X.-X. Zhang, and X.-D. Wang, “Multi-objective and multi-parameter optimization of a thermoelectric generator module,” *Energy*, vol. 71, pp. 367–376, 2014.
  - [32] Z. Liu, S. Zhu, Y. Ge, F. Shan, L. Zeng, and W. Liu, “Geometry optimization of two-stage thermoelectric generators using simplified conjugate-gradient method,” *Applied Energy*, vol. 190, pp. 540–552, 2017.
  - [33] Z.-Z. He, “A coupled electrical-thermal impedance matching model for design optimization of thermoelectric generator,” *Applied Energy*, vol. 269, p. 115037, 2020.
  - [34] G. Fraisse, J. Ramousse, D. Sgorlon, and C. Goupil, “Comparison of different modeling approaches for thermoelectric elements,” *Energy Conversion and Management*, vol. 65, pp. 351–356, 2013.
  - [35] A. Chakraborty, B. Saha, S. Koyama, and K. Ng, “Thermodynamic modelling of a solid state thermoelectric cooling device: Temperature–entropy analysis,” *International Journal of Heat and Mass Transfer*, vol. 49, no. 19, pp. 3547–3554, 2006.
  - [36] E. M. Ledesma, S. Sammak, and M. M. Barry, “Modeling bridgman heating in thermoelectric generators,” in *ASTFE Digital Library*, Begel House Inc., 2021.
  - [37] P. J. Roache, “Perspective: a method for uniform reporting of grid refinement studies,” *Journal of Fluids Engineering*, vol. 116, no. 3, pp. 405–413, 1994.
  - [38] C. J. Roy and W. L. Oberkampf, “A comprehensive framework for verification, validation, and uncertainty quantification in scientific computing,” *Computer Methods in Applied Mechanics and Engineering*, vol. 200, no. 25, pp. 2131–2144, 2011.
  - [39] I. B. Celik, U. Ghia, P. J. Roache, *et al.*, “Procedure for estimation and reporting of uncertainty due to discretization in cfd applications,” *Journal of fluids Engineering-Transactions of the ASME*, vol. 130, no. 7, 2008.